Realizing Photo-sieving: A Novel and open source UAV-SFM Algorithm for Grain Size distribution Maps of coarse particles

Lovati Marco, Fan Xuanmei*, Yang Dongxu, Wang Dongpo, Zhang Binlang, Danny Love

Wamba Djukem, Xu Qiang

Abstract

GSD (grain size distribution), constitutes a paramount parameter for comprehending the behavior and dynamic mechanics of mass movements, such as debris flows, rock avalanches, sediment transport etc. Alongside traditional sieving methodologies, the past few decades have witnessed a growing interest in photo-sieving, the technique of deducing GSD directly from photographic data. Photo-sieving holds promise for augmenting the spatial and temporal resolution of superficial GSD analysis by virtue of its accessibility, reduced labor intensity, and non-invasive nature. Moreover, the integration of aerial photography within the discipline enables to include the coarse-grained fraction, expanding the scope of particle size analysis beyond the capabilities of traditional sieving. This study introduces a novel algorithm for extracting the coarse-grained fraction using UAV (unmanned aerial vehicle) photography. This novel approach enables us to analyze hectare-scale extents, probing tens of thousands of clasts - surpassing previous similar techniques by two orders of magnitude - and generates a detailed map of the position and dimensions of each individual particle within the sedimentary system. Furthermore, the algorithm exhibits remarkable resilience in navigating real-world complexities, effectively discerning clasts from vegetation, anthropogenic artifacts, and handling exceptionally large boulders, rendering it suitable for application in diverse field settings. We anticipate that this technique could become a valuable tool for advancing our understanding of debris flow and rock avalanche dynamics, sediment transport processes, and the stability of landslide dams.

Plain Language Summary

Knowing the sizes of the different grains in a landslide or river helps us understand how it moves and changes. Besides sieving the material, scientists are now using photos to extract size information. Capturing pictures from flying drones helps us study larger rocks, which could not have been done with sieves. The new method in this paper lets us survey vast rock-covered areas, much larger than ever before. We can automatically examine tens of thousands of individual particles, this gives us a detailed map of where and how big each rock is. Our tool is effective at extracting size information, even in the case of plants, buildings, and exceptionally large boulders in the photo. This new way of studying sediments could help us understand their speed, how they travel, and even how stable and durable they are.

37

38 **Keywords**

39 Grain size distribution, image segmentation, SFM photogrammetry, photo-sieving, unmanned
40 aerial vehicles, open-work unconsolidated sediments.

Highlights

- Available techniques to map coarse particles (gravels to boulders) on a large scale are still significantly reliant on a sampling process.
- We created a novel algorithm for extracting the coarse-grained fraction using UAV (unmanned aerial vehicle) photography.
- Our model generates data for training a Mask R-CNN algorithms, unlocking further improvements in Grain Size Distribution surveys.

1. Introduction

In the scope of sedimentological analysis, there has long been a fundamental drive toward comprehending the grain size distribution (GSD). Particle size is a critical sediment trait for interpreting geological deposits, designing flood protection measures (Habersack et al., 2011), and assessing slope stability (Duna et al., 2017). Likewise, the geotechnical characterization of landslide dams is strongly correlated with the grain size distribution of their constituent materials. Specifically, grain size influences landslide dam stability by controlling the strength and permeability of the dam material, and it affects the hydrograph resulting from the dam failure (Casagli et al., 2003; Fan et al., 2021a,b) (see Figure 1). Mapping the distribution of coarse clasts within rock avalanche deposits can provide valuable insights into their dynamics mechanism. Characterizing the carapace, the coarse-grained outer shell of rock avalanches, provides key insights into how lithological and morphological variations influence rock avalanche dynamics (Dufresne et al., 2016) and (Duna et al., 2017). Traditional methods for directly measuring rock avalanche deposits have faced significant limitations due to factors such as sampling challenges (Dunning, 2006).

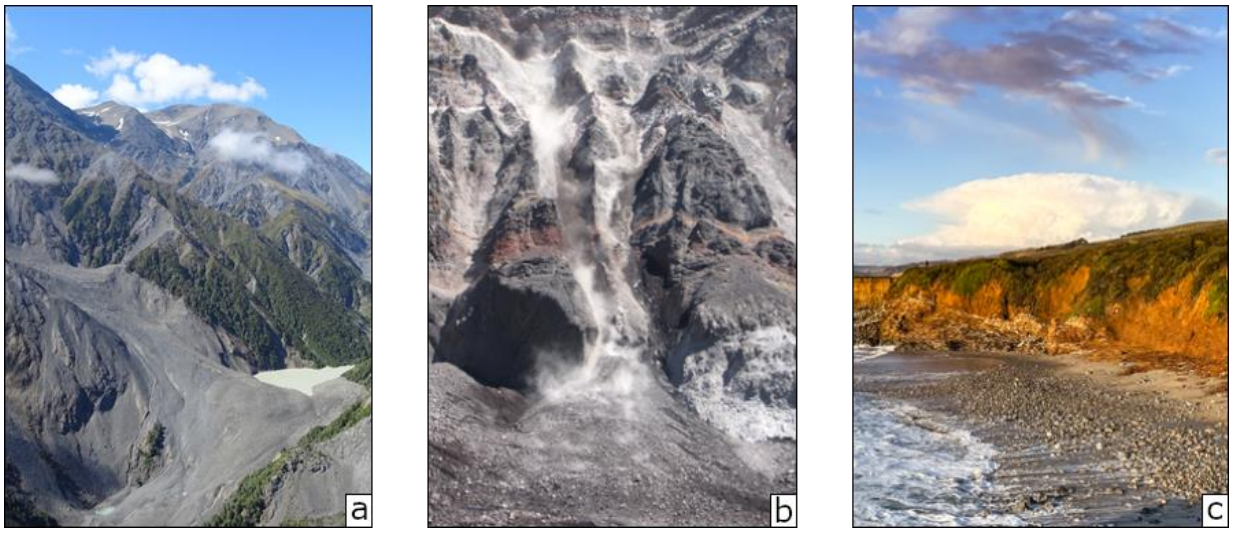

Figure 1. Some of the most promising potential scientific breakthroughs of the present algorithm. The example pictures represent: a) Landslide-dammed lake in the headwaters of the Hapuku River in the Seaward Kaikoura mountain range in New Zealand, credit to Jonathan Godt. b) Steep 600 m high rockfall descending the crater of Mount St. Helens, credit to Andy Barsotti. c) Geological features along the Californian coastline that are shaped by varied coastal processes, credit Meaghan Faletti. Photos taken from https://www.usgs.gov/media/images, all photos are in the public domain.

GSD analysis have been performed since the dawn of geological surveys, at the beginning of the XIX century, as it is useful for characterizing and understanding transport and deposition mechanisms in mass movements such as fluvial sediments, landslide deposits and debris flow deposits. For non-cohesive bed material, the GSD and its characteristic deciles (e.g., D_{10}, D_{50}, D_{90}) are critical parameters for simulating hydraulics and sediment transport (Bunte and Abt, 2001). (Meyer-Peter & Müller, 1948) define D_m as the mean diameter weighted by the fraction of particles of a given size, and D_{90} is the particle diameter at which 90% of the particles by mass are smaller e.g. Tritthart et al. (2011). Many deterministic models attempt to model the mechanical behaviour of unconsolidated sediments by considering the median percentile D_{50} of the cumulative grain size distribution. However, the fiftieth percentile is often a poorly representative grain size class (Casagli et al., 2003). The particle size distribution is also important for other factors, such as: to delineate aquatic habitat types, interpret geological deposits, designing flood protection measures and assessing sediment stability (Habersack et al., 2011; Casagli et al., 2003) .

Traditional laboratory sieving for sediment classification is a labour-intensive and time-consuming process, requiring skilled personnel and meticulous technique. Despite the importance of determining the grain size distribution of landslide dams, because traditional sieve analyses are impractical for materials with such a wide range of particle sizes, there are few quantitative studies on the topic (Casagli et al., 2003). Additionally, the entire process of sediment collection, transportation, and sieving can be expensive. In alternative, a variety of in situ methods have been developed to acquire particle size distributions, e.g. based on the enumeration of individual sediment particles along a grid (Wolman, 1954) or transect (Fehr, 1987). For an exhaustive review of conventional sampling techniques, please refer to (Bunte & Abt, 2001). Despite their widespread use, these methods are time-consuming, often inaccurate, and difficult to apply in wetted beds or gravel bar islands.

One promising approach to expedite data collection is to leverage photographic analysis to infer GSD. Manual particle size estimation from ground-level images, also called photo-sieving, was pioneered in the late 1970s (Adams, 1979; Ibbeken and Schleyer, 1986). Despite potential inaccuracies in estimating the size

of individual grains, image-based sampling offers several advantages, including improved transparency, reproducibility, and efficiency.

Photo-sieving exclusively captures the outermost GSD, as camera-based observation is inherently unable to unveil particles concealed beneath surface layers. Despite this constrain, photo-sieving's inception in the late 1980s marked the beginning of a trajectory of refinement. This trajectory of refinement, marked by the promise of a collection of advantageous attributes, is evident as shown in Harvey et al. (2022).

- Photo-sieving can encompass a broader spectrum of grains compared to traditional sieving. While conventional sieving excels in evaluating the finer sediment fraction, its application for incorporating pebbles or larger particles necessitates supplementary techniques for comprehensive analysis.
- Photo-sieving accelerates sediment analysis, enabling comprehensive surveys of expansive terrains without the need for sample selection (Lang et al., 2021). This increases spatial and temporal resolution, and the lack of spatial sampling facilitates the detection of spatial variability across the sediment surface.
- Photo-sieving is non-invasive, allowing iterative surveys of the same region without disturbing the sample. This makes it compatible with high temporal resolution studies. Additionally, photo-sieving can be used before other, more invasive survey methods, enabling comparative analysis of different techniques.
- Photo-sieving provides an effective tool in emergency survey, and aligns with independent replication endeavours due to its suitability for online sample sharing and duplication.

In recent years, several automated methods have been developed to extract characteristic grain size parameters from digital imagery and laser scanning data. GSD analysis from imagery can be broadly categorized into two approaches: statistical correlation and object-based approaches.

The statistical correlation methods involve extracting textural features from image patches and correlating them with the median or average grain size. This eliminates the need for individual clast identification and

measurement, saving time. Pioneered by Carbonneau et al. (2004), effective grain size analysis expanded through Heritage and Milan (2009) adapting methods to terrestrial laser scanning, and Buscombe et al. (2010) refining techniques for improved accuracy and efficiency. Buscombe (2013) and others advanced statistical correlation approaches, integrating machine learning and CNNs for grain size distribution estimation. SediNet, a CNN-based framework proposed by Buscombe (2020), utilized a dataset of 409 manually labeled sediment images for training. Lang et al. (2021) introduced a deep learning model inspired by HistoNet (Sharma et al., 2020) to directly predict absolute size distributions without explicit object detection, modeling empirical distributions through maximum likelihood estimation. Statistical correlation methods for particle size determination from imagery often face a common limitation: the need for empirical calibration data to establish predictive relationships between image features and grain size. The accuracy of these methods relies on the quality and size of the calibration dataset, posing limitations across diverse orders of magnitude in GSD. This constraint becomes evident, especially for sizes larger than the model calibration. Moreover, these methods are susceptible to failure when external objects, like vegetation or artifacts, affect the texture under analysis. Additionally, approaches lacking grain detection via image segmentation cannot generate labeled datasets for specific segmentation algorithms, such as Mask R-CNN (He et al., 2017), hindering future applications.

Object-based approaches entail detecting and measuring individual clast objects through visual or automated image processing techniques. Pioneering methods involved manual clast identification and measurement in terrestrial photographs for particle size determination. Automated approaches, developed over time by various authors, use object-based image analysis, segmenting images based on spectral, spatial, and textural characteristics. In particle size determination, these techniques segment clasts into objects, often fitted to ellipsoids for estimating their longest and second-longest diameters (i.e. the characteristic lenght). These are commonly used to describe particle size under the assumption that the shortest diameter lies perpendicular to the ground due to the effect of gravity. Recent advancements in object-based image analysis, building on earlier work by (Butler et al., 2001; Graham et al., 2005a; Graham et al., 2005b), were made by (Detert &

Weitbrecht, 2012) and (Graham et al., 2010). (Graham et al., 2005) used grayscale thresholding to segment a binary image, distinguishing grains from voids. (Graham et al., 2010) introduced a double-thresholding approach for interstitial segmentation, combining grayscale thresholds and a bottom-hat filter, with final segmentation using a watershed algorithm. (Detert & Weitbrecht, 2012) enhanced the methodology through modifications like image preprocessing, additional filters for interstice detection, and post-processing manipulation of grain elements via a graphical user interface (GUI).

A fundamental commonality between statistical correlation and object-based approaches to particle size determination from imagery is that they both measure particle size in image pixel units. At some point in the processing pipeline, both approaches must convert these pixel dimensions to physical units, based on meters, using the known image scale and/or pixel dimensions. For terrestrial imagery, a common method for establishing image scale is to include a scale object (usually a ruler or a coin) in the photographs. For airborne imagery, the nominal altitude above ground level (AGL) is used. The image scale is the ratio of the distance between two points in the image to the corresponding distance on the ground. It is calculated by dividing the nominal AGL by the focal length of the camera used to acquire the image. In the case of drone imagery, the precise altitude above ground level (AGL) is often difficult to determine, which means that the spatial resolution of the imagery is not known in advance. The precise determination of image scale for each image in a small unmanned aerial vehicle (UAV) has been the main challenge solved by Carbonneau et al. (2018).

A separate category of studies has investigated the analysis of 3D point cloud data instead of the images (Wu et al., 2018). This data is acquired using remote sensing techniques, such as terrestrial laser scanning (TLS) (Brasington et al., 2012), airborne laser scanning (ALS) (Huang et al., 2018), and photogrammetry (Vázquez-Tarrío et al., 2017). These techniques provide dense and accurate 3D data that can be used for a variety of applications, including mapping, surveying, and monitoring. Processing 3D point cloud data is computationally more expensive than processing 2D imagery due to the increased complexity of the data. Terrestrial lidar data acquisition is less flexible and scalable than airborne lidar, due to the need to move the

sensor around to capture data from all angles. Additionally, airborne lidar is still expensive, although it is expected to become more affordable as consumer-grade UAV-based lidar systems become more widely available. Photogrammetric 3D reconstruction produces point clouds with lower resolution than the original images, which can obscure smaller features even when flying at relatively low altitudes. (Woodget et al., 2018) argued that image-based texture analysis is more effective than roughness-based methods for characterizing small grain sizes.

Photo-sieving has already expanded our ability to measure superficial grain size distribution (GSD). However, the most desirable attributes are still partially or fully unrealized. Often, a combination of approaches has been used to address the limitations of individual methods (Harvey et al.,2022).

Our approach revolutionizes the element separation phase in automated grain detection: by eliminating the need for a final manual correction, our work enables particle separation on a much larger scale. This milestone is achieved by incorporating Structure-from-Motion (SFM) photogrammetry into the element separation instead of the final re-scaling phase, enabling separation to be confirmed from different viewpoints.

The improved capability of mapping pebbles and boulders would offer valuable insights into transport mechanics both in fluvial and coastal environments, which are mutually interconnected (Warrick et al., 2019). It could refine both the estimation of river sediment budgets (Fang et al., 2017) and the understanding of coarse clast influence on shoreline resistance to waves and storm surges (Irvine et al., 2006). Furthermore, it could provide additional controlling variables, besides present ones such as volume or height drop, in statistical analysis that explain rock avalanche mobility (Strom et al., 2019)

2. Methodology

2.1 Overview

The methodology elucidated in this paper may, at first glance, bear semblance to the approach presented in the work of Carbonneau et al. (2018). However, a key distinction exists: rather than relying on manual intervention by the user for correcting the misdetections, our method harnesses automated processes, leveraging a sparse point cloud model (as delineated in Figure 2 and Section 2.1) to compare identical locations from multiple vantage points. While employing SFM photogrammetry in its workflow, (Carbonneau et al., 2018) does not use the 3D mesh for detection, but for rescaling only, as declared in the conclusions: *"photosieving can now be deployed without the presence of rulers"*, *"meaning that the pilot and field crew do not need direct access to the sample location"*. Figure 2 provides a high-level (i.e. semantic) depiction of the workflow: it begins with a collection of photographs capturing the sediment under study. These images necessitate adequate overlap, ensuring that elements within the frames are captured from multiple angles. This is necessary to perform SFM photogrammetry (see Section 2.2.2).

As of the writing of this manuscript, the yield from SFM photogrammetry is a sparse point cloud—a collection of points in three-dimensional space (see section 2.2.2). Each point within this assembly is characterized by its spatial coordinates in 3D, accompanied by a list of 2D pixel-based coordinates, each signifying its position across one of the photographic frames. This unique dataset facilitates the matching of congruent regions across distinct images, thereby affording a multi-perspective vista of the sediment.

Upon the identification of a specific zone containing a distinct assortment of boulders and pebbles, the process of object detection (as elaborated in section 2.2.3) is executed from various vantage points. Within each object detection cycle, a number of objects are prone to erroneous identification due to both over-segmentation and under-segmentation. In traditional procedures, these misidentified image segments would necessitate manual correction by the user. While undeniably quicker than manual separation, this method imposes constraints on the volume of separable pebbles, rendering a comprehensive survey of an entire

drainage basin a laborious endeavour. In our approach, we project five pivotal points (comprising the centroid and the extremities of the longer and shorter axes) from the photographic plane onto the mesh of the sparsely populated point cloud. Notably, both accurate detections and erroneous ones are gathered over the same mesh. Since the accurate detections demonstrate a higher degree of consistency across diverse viewpoints in comparison to the erroneous ones, we leverage a clustering algorithm (detailed in section 2.2.4) to discern and subsequently eliminate the instances of misidentification.

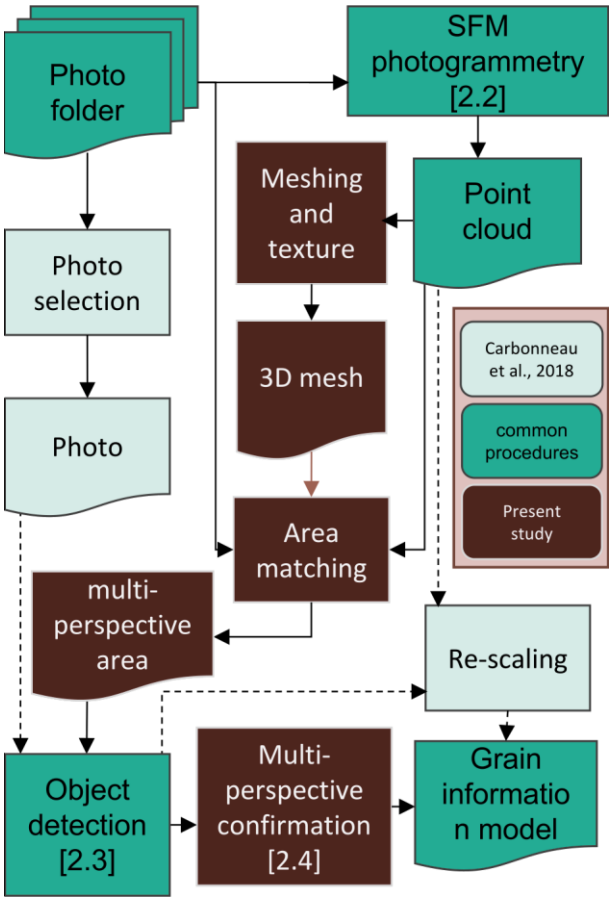

Figure 2. high level/semantic flowchart of the entire workflow, and key difference with (Carbonneau et al., 2018)

2.2 Structure from motion (SfM) photogrammetry

Structure from Motion (SfM) photogrammetry is a robust technique employed in geospatial and scientific research to derive a three-dimensional representation from a series of overlapping two-dimensional images, here acquired from UAV. This method achieves the reconstruction of scenes or landscapes in an accurate, yet cost-effective manner.

In SfM photogrammetry, a set of images is captured with a camera or sensor, ensuring sufficient overlap between consecutive frames (in our example 80% overlap in both directions of flight). Initially, feature points or key points are identified within the images, often employing techniques like Scale-Invariant Feature Transform (SIFT) or Speeded-Up Robust Features (SURF). These key points are then matched across the images to establish corresponding points in multiple views.

Once the correspondence between key points is established (see the feature point in green in Figure 3b the software retrieves camera poses from the EXIF (EXchangeable Image File format) data, which represent the position and orientation of the camera for each image. This information forms the foundation for the creation of a sparse point cloud, which is the representation of the 3D structure of the scene used in this study.

Typically, to enhance accuracy and completeness, dense point cloud generation is pursued, wherein additional points are interpolated between the sparse points. Subsequently, the derived dense point cloud is used to construct a highly detailed and geometrically accurate 3D model of the subject. Due to resource and time limitations, for the present study, this passage has not been integrated. This study has been conceived as a radically innovative workflow; although it has already yielded some degree of success, it necessitates several subsequent iterations for refinement before attaining the level of conclusiveness warranted for widespread adoption. Our workflow directly refines the sparse model through mesh generation and texture mapping to produce a visually realistic representation (see Figure 3a). While the integration of dense point production undeniably holds potential for enhancing spatial accuracy in the analysis, this study, as

elucidated in the paper, has predominantly prioritized the mitigation of segmentation errors. Consequently, emphasis has been directed toward optimizing other facets within the workflow.

Figure 3. (a) Rendering of sparse SfM model after mesh generation and texture mapping. Notice how the truck on the right side of the image has not been included in the mesh but is simply part of the texture (as captured in the photograph). This is due to the fact that it was moving, thus has not been able to generate feature points. (b) The working principle of Structure From Motion (SFM) photogrammetry involves identifying known elements (represented in green) in multiple images. When the same point, known as a feature point, is recognized across these images, and the camera's location during each shot is known, precise triangulation and geolocation of the feature point can be achieved

In conclusion, Structure from Motion (SfM) photogrammetry, by leveraging the principles of image matching, and point cloud generation through camera pose, enables the creation of detailed 3D models from 2D image data (see Figure 3 b).

2.3 Automatic object detection

The automated object detection methodology integrated into our workflow demonstrates minor disparities when compared with the procedure shown in Detert and Weitbrecht (2012), an approach we strived to replicate employing Python in lieu of the original Matlab script. The work of Detert and Weitbrecht proposes a systematic approach for extracting the grain size distribution within a sediment bed through the

analysis of its digital top-view imagery. This procedure stands out due to its efficacy in the separation of elements when compared to previous methodologies, and, to the best of our knowledge, still occupies the pinnacle of image segmentation for granulometric analysis.

In the broader context of this method, the specific procedure encompasses three distinct stages: interstice detection, foreground detection, and subsequent separation through the application of watershed segmentation. The initial image (depicted in Figure 4a) undergoes a sequence of pre-processing steps, including conversion to greyscale, histogram equalization, and Gaussian filtering for the purpose of smoothing the textural irregularities associated with the clast surfaces. The identification of interstices is accomplished through the application of a confirmed adaptive Otsu thresholding technique (illustrated in Figure 4b).

In this methodology, the Otsu threshold value is computed over a matrix of sub-sampled regions (cells) within the original image. The resultant matrix is subjected to Gaussian filtering to mitigate abrupt variations in cell values. This strategic processing serves to eliminate the inadvertent inclusion of entire darker regions within the image as interstices, thereby enhancing the discernment of genuine interstices within shaded areas or areas characterized by darker average coloration. The nomenclature 'confirmed' is ascribed to the Otsu threshold, as it is applied iteratively, considering two distinct proportions of interstices: a more inclusive and a more exclusive one.

The inclusive definition of interstice is adopted, but only in cases where it encapsulates an exclusive interstice within its core, thereby facilitating a refined differentiation between noise artefacts and authentic interstices amid the pebbles. Figure 4 b visually represents the inclusive 'confirmed' areas in grey, whereas the exclusive areas are represented in black.

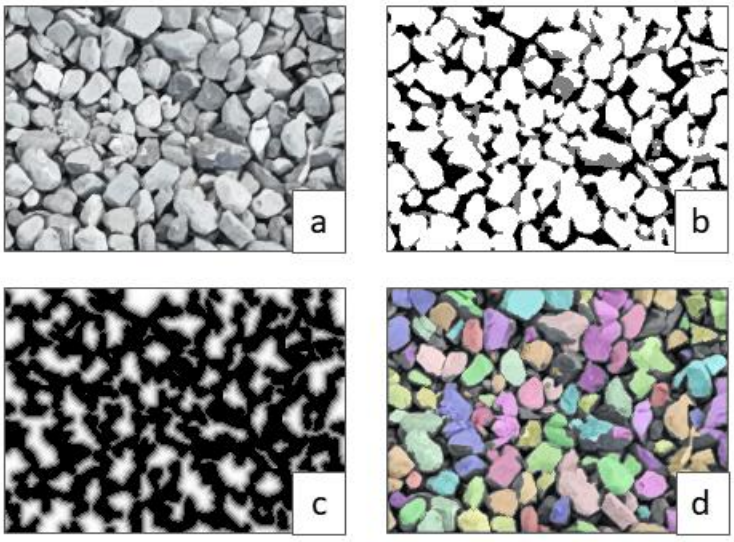

Figure 4. significative steps during the automatic grain detection workflow

At this stage, a substantial portion of interstitial spaces has been identified; however, a considerable number of pebbles remain clustered. It is evident that there exists a delicate balance between comprehensively recognizing interstices and the potential for overestimation due to misinterpreting certain shadows as interstitial spaces. To address this challenge, as shown in Detert and Weitbrecht (2012), we postulate that two or more adjacent pebbles, still coalesced, may be discerned by identifying a chokepoint corresponding to their actual interstice. Consequently, for the delineation of separate foreground seeds, the segments not constituting interstices (depicted in white in Figure 4 b) are subjected to a distance transform process (as shown in Figure 4 c), followed by separation using Otsu filtering.

In the final step, all regions identified as foreground serve as initial seeds for a watershed segmentation procedure. This process confines the unknown regions by utilizing the recognized interstices (as depicted in Figure 4 b) and the foreground seeds.

While Detert and Weitbrecht (2012) significantly advanced the domain of image-based superficial GSD analysis, serving as a cornerstone for UAV surveys, a fundamental limitation becomes apparent. Specifically, a delicate balance exists between the risks of under-segmentation and over-segmentation. Consequently, in

addition to the imperative need for calibration, as indicated by the authors who state, "*six parameters are chosen to steer the watershed separation process, and the optimum ranges were found by empiricism*" (Detert and Weitbrecht, 2012, p. 597), it necessitated the inclusion of a manual post-processing phase to rectify segmentation errors. As articulated by Detert and Weitbrecht (2012) on page 595, this post-processing phase involved handling individual grain elements through a Graphical User Interface. This intervention was crucial to ensure the accuracy and reliability of the results.

2.4 Multi perspective confirmation

The key innovation of the proposed workflow is to automate the final manual step in the element separation stage of object detection, a limitation of prior work Carbonneau et al. (2018), enabling particle detection at an unprecedented scale. We achieve this milestone by integrating SFM photogrammetry into the element separation phase of the workflow, rather than the final rescaling phase (see Figure 2), enabling the confirmation or dismissal of potential clasts from multiple viewpoints. Both accurate and erroneous detections are aggregated on the same three-dimensional mesh. Because accurate detections exhibit greater consistency across disparate viewpoints than erroneous ones, we employ a clustering algorithm to identify and remove misidentifications. For a given area of interest, we collect all viewpoints of that area, and analyse them using the procedure outlined in Section 2.2.3, which is adapted from Detert & Weitbrecht (2012). We project each clast detection onto the sparse point cloud mesh as five characteristic points: the centroid, the extrema of the major axis, and the extrema of the minor axis. At this stage, the mesh contains many potential detections, some of which are false positives, while others represent actual clasts present in the area.

The separation of genuine detections from false positives in GSD curves involves a trade-off between the risk of including false positives and the loss of true clasts. This is because, although true detections are more reproducible than false detections, they are not perfectly repeatable, due to systematic and random errors introduced during the workflow (e.g., parallax errors, differences in axis lengths caused by varying viewing

angles, and triangulation approximations). Conversely, false detections may exhibit some degree of consistency with each other, or may simply resemble instances of true detections. An algorithm that requires high consistency to confirm a detection may discard valuable data and identify a sparse subset of the previously separated clasts, while an algorithm that is too permissive may reduce the accuracy of the detection by including computational errors among the confirmed clasts. To address this trade-off, a two-pronged approach has been employed. Initially, a basic filtering algorithm is employed to eliminate the most evident misdetections, as demonstrated in Table 1. Following this, a RF (random forest) algorithm is used to further refine the results and create the final model, see Figure 5.

Table 1. Sankey diagram of the first phase of the confirmation and relative parameters.

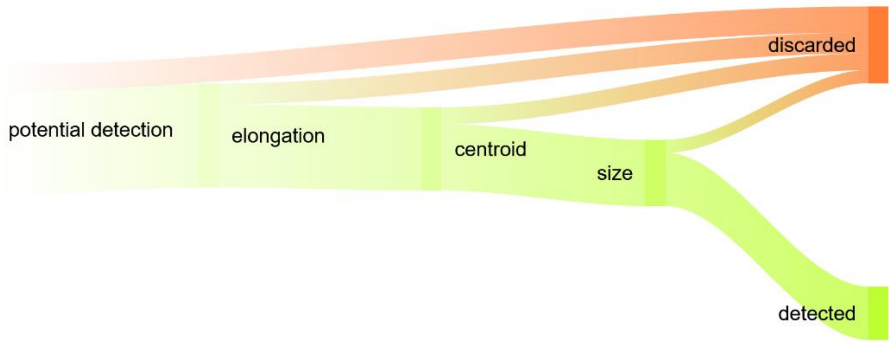

condition	description	parameters
elongation	Unnaturally elongated clasts, where the longest diameter is more than **O** times the smaller diameter, will be considered misdetections.	**O = 3.5**
centroid	Clasts are discarded if their center is close to fewer than **m** other centers from distinct independent segmentations. Where 'close' is defined as being within **d** times the smaller diameter of the median potential detection.	**m = 5, d = 0.25**
size	From the clasts meeting the centroid condition, we will exclude nearby clasts whose difference in shorter diameter exceeds **l** times the shorter diameter of the median potential detection. If the entire cluster contains fewer than **m** potential candidates, it will be discarded.	**l = 0.4, m = 5**

The initial stage of selection is a cascade of filters that eliminate the most evident misdetections. Consequently, it is designed to preserve a significant number of potential clasts, even if some false detections remain. Initially, it eliminates all clasts with excessive elongation. Clasts with an aspect ratio greater than 3.5 are discarded (see elongation condition in Table 1). Excessive clast elongation could be caused by triangulation errors when projecting the clast from the image plane, where it is detected, to the 3D

mesh. This issue is primarily caused by the mesh's current inaccuracies. It would be significantly less severe if a denser mesh were used, but this would restrict the method's applicability to GPU-equipped devices. After eliminating excessively elongated clasts, the algorithm iteratively examines the remaining candidates, counting, from each centroid of the object under analysis, the centroids of other detections. Clast from other viewpoints within a close proximity to the centroid of the clast under analysis are considered. The underlying principle is that other viewpoints that record a centroid in close proximity to the one being analyzed are likely to be different views of the same object. All clasts that do not accumulate at least 5 centroids within a specified radius are rejected. In other words, clasts with fewer than five spatial confirmations are discarded. According to the centroid section of Table 1, a centroid is considered close if it is located within 0.25 times the shorter diameter of the median potential detection. To be confirmed, it is not sufficient for a centroid to be close to another detection; the characteristic radius (i.e., the minimum distance between the centroid and the edges of the clast) must also be within a specified threshold. Therefore, all potential confirmations with a characteristic radius that differs significantly from the one being analyzed are discarded. If the number of confirmations falls below 5 after applying this additional filter, the clast under analysis is eliminated (see size condition in Table 1).

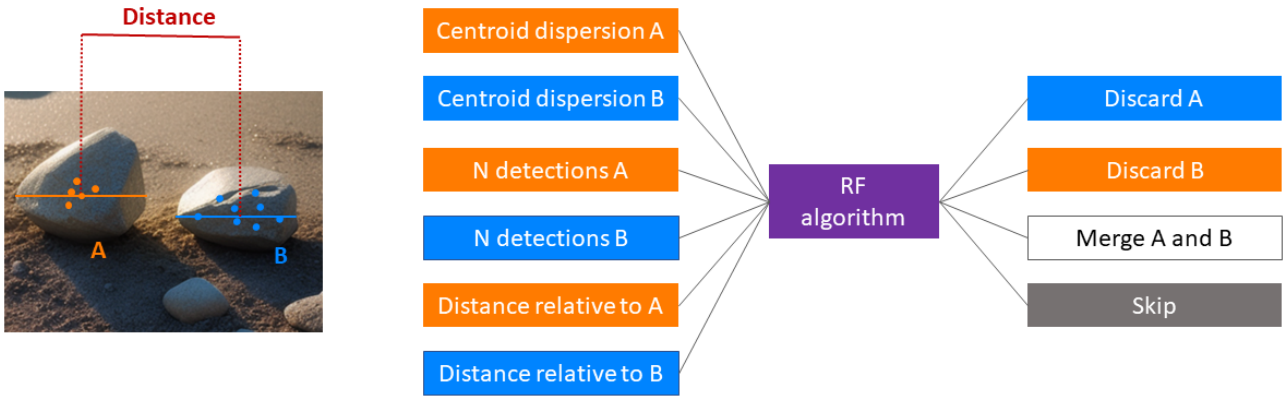

Figure 5. input and categories of the RF algorithm used to refine the discrimination between true and false detections

The second stage commences after the crudest errors have been rectified. The necessity of the second stage arises from the existence of misdetections that originate from systematic errors, such as transposition issues from the photo plane to the 3D mesh, or especially challenging clasts to separate. For such misdetections, a

simplistic filter such as the one presented in Table 1 will inevitably succumb to the aforementioned trade-off between rejecting genuine detections and retaining misdetections. The second stage of the clustering algorithm leverages a Random Forest (RF) algorithm to resolve situations where two or more potential clasts overlap. The RF algorithm ingests a set of inputs (see Figure 5) and determines whether to discard one of the potential clasts, merge them, or maintain the status quo. The algorithm ingests a total of 6 inputs, divided into 3 features for each of the two conflicting clasts being analysed. The first feature is the centroid dispersion (see Figure 5), which is the mean distance between each centroid within the cluster representing the detection. According to Table 1, a detection is confirmed when there is a cluster of at least 5 centroids that are sufficiently close to be considered coincident. However, once the first stage threshold is met, the accuracy can vary, so these variations must be considered when resolving conflicting potential detections. The second input is the number of detections, which must be at least 5 to meet the first stage clustering threshold. Once this threshold is met, some detections may have significantly more instances than others, indicating a higher degree of consistency. The third feature is the relative distance, which is designed to handle cases where a smaller stone is merged with a much larger one. The image segmentation phase (see Figure 4d in Section 2.2.3) uses a distance transform to identify choke points in inter-interstitial regions. A common failure mode occurs when a small stone is not perfectly separated from a larger one. In such cases, the maximum distance from the interstices to the core of the small stone is negligible compared to that of the larger stone, resulting in the entire small stone being merged with the larger stone as if was a morphological feature. The RF algorithm is trained to preserve the smaller clast, input ‘skip’ in Figure 5, whenever it detects this situation based on the combination of the two relative distances.

It is worth mentioning that there is an extremely large search space when selecting the combination of features that can be treated as input for the second clustering stage, thus there are abundant margins for performance improvement.

3. Accuracy evaluation

3.1 Preparation of the dataset

The sediment chosen to test our new technique (see Figure 3) constitutes a section of the Banzi gully debris flow, which occurred on August 20, 2019, as part of a cluster of debris flows triggered by heavy rainfall. The Banzi Gully debris flow was one of the largest and most destructive of the cluster, causing significant damage to infrastructure and property. The debris flow buried houses, roads, and bridges, and damaged several roads and dams. The Banzi Gully debris flow caused significant damage to infrastructure and property, and resulted in the deaths of 16 people and the displacement of over 48,000 people. The economic losses caused by the debris flow were estimated to be over 3.4 billion RMB (Lyu et al.,2022; Zhang et al.,2023; Li et al., 2021; Wang et al., 2022). The Chinese government has implemented a number of debris flow hazard mitigation measures in the Wenchuan area since the 2019 debris flow event. These measures include replanting vegetation, constructing engineering structures, and developing early warning systems. The government has also provided financial assistance to people who were affected by the debris flow. In literature several mitigation strategies for avoiding similar events in the future have been evaluated: Zhang et al (2022) have evaluated the efficacy of geotechnical and ecological control engineering elements working in unison, He et al (2022) have evaluated geological control engineering projects in terms of direct and cascading effects.

We deployed a DJI Mavic drone equipped with a standard Hasselblad L2D-20c camera to an altitude of approximately 100 meters to image the debris sediment. In future experiments, we will lower the altitude to improve the detection resolution, while maintaining the safety of the drone as our primary concern. Alternatively, higher image resolution can be achieved by flying the drone at a higher altitude while using a longer focal length camera gimbal. Top-down aerial imagery of the sediment was acquired at a regular interval to maintain a constant 80% overlap between adjacent images. The typical output of the procedure is shown in Figure 6.

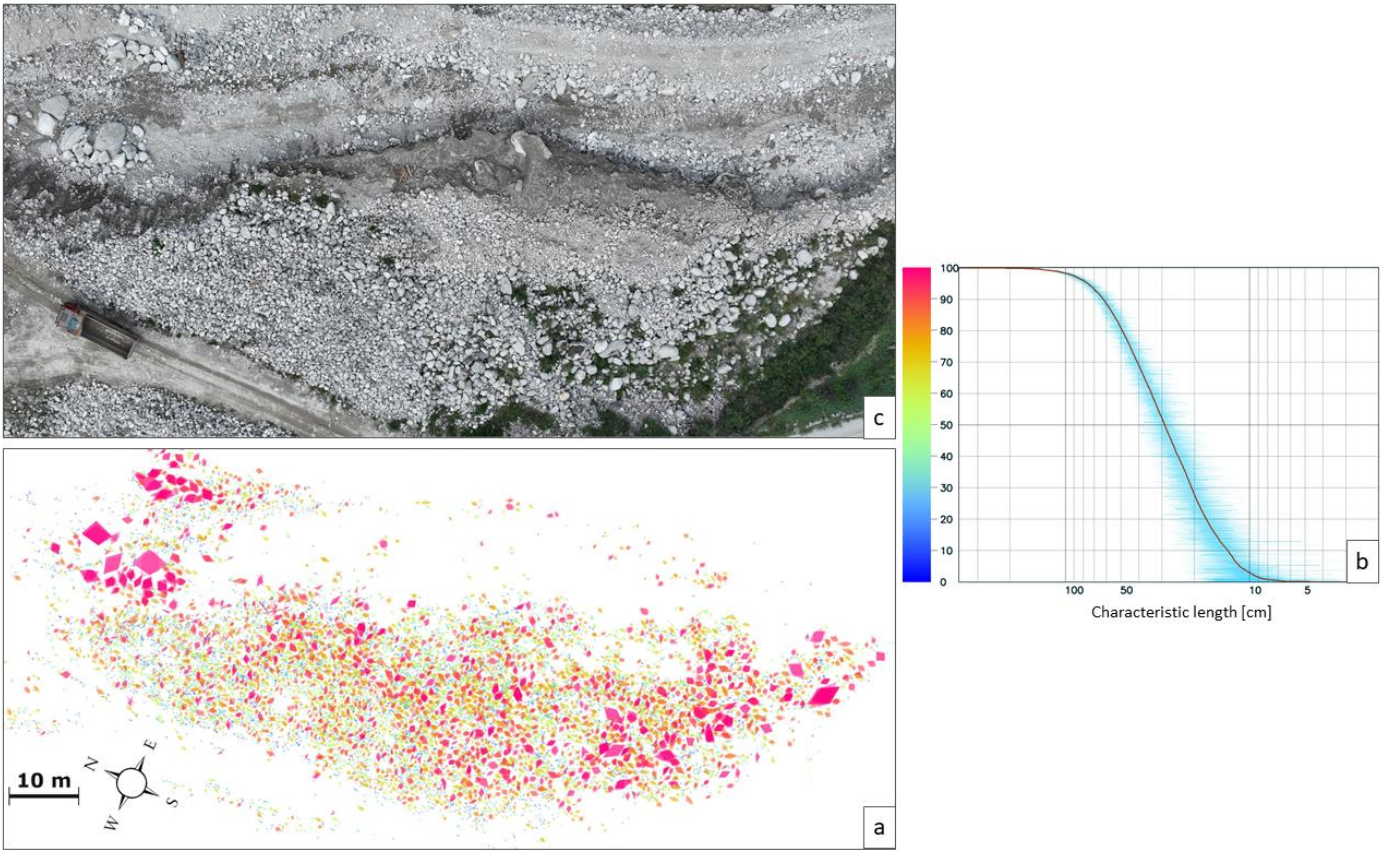

402

403 *Figure 6. (a) map of the clasts over the entire catchment, (b) grain size distribution curve with color code of the characteristic lenght, (c) top-*
404 *down view of the catchment*

3.2 Comparison with a manually analysed sample

To assess the detection accuracy of the proposed method, we selected three representative samples from the analysed area (see Figure 7 a) and superimposed the detection model on snippets of aerial photography to visually evaluate the fidelity of the clast layout reproduction. Because the proposed method is designed to automate tasks that have been traditionally performed by human experts, we applied the line sampling technique (Fehr, 1987) to the selected samples and compared the resulting partial GSD curves to the manually generated curves.

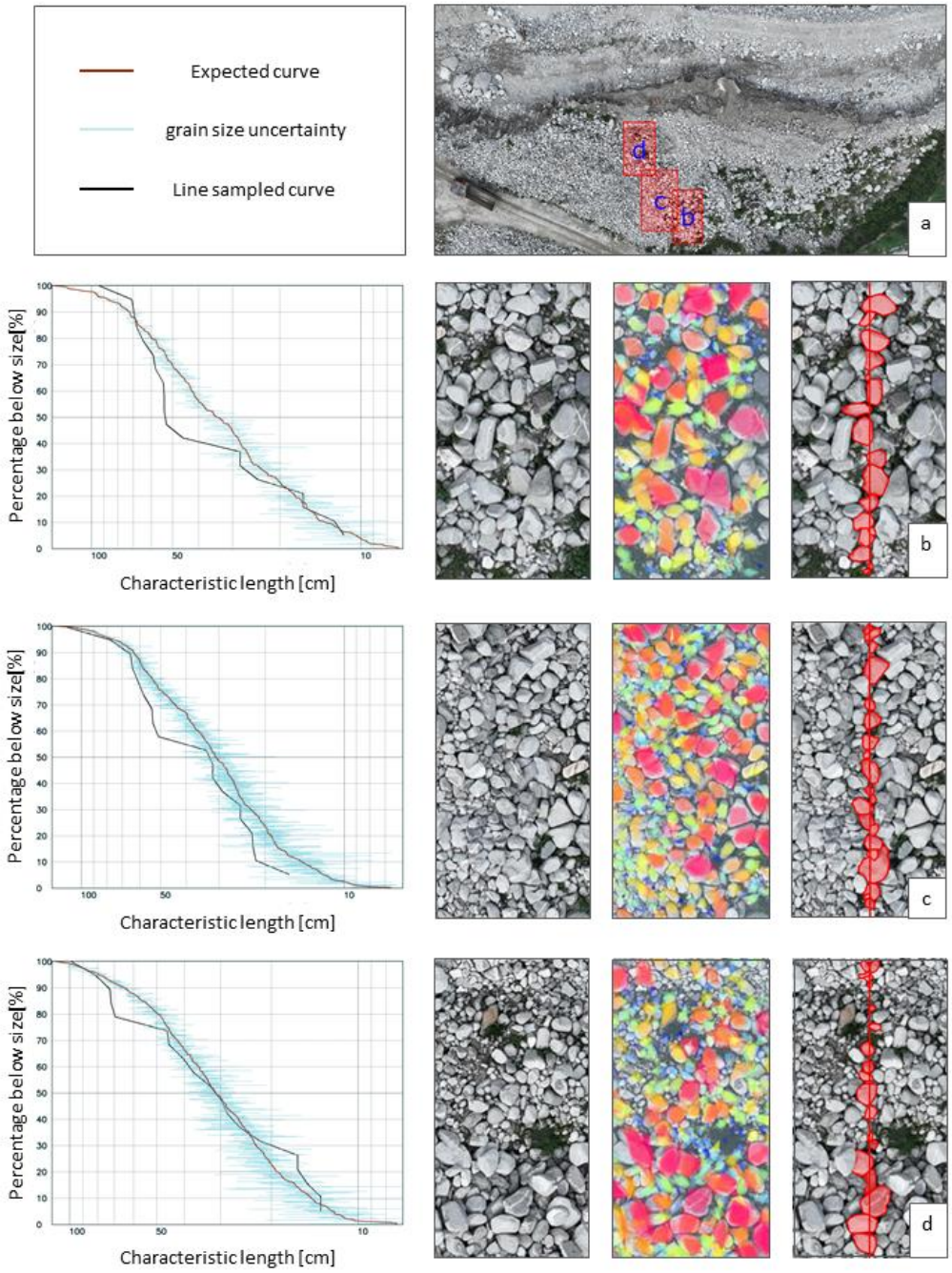

Figure 7. analysis of the GSD in three samples out of the analyzed area. (a) aereal photo with highlight of the location of the samples. (b to d) automatically generated distribution curve vs Fehr sampling and relative visualizations

Figure 6 presents the overall catchment layout, revealing the software's accurate perception of the gully's large-scale spatial distribution. The largest boulders are organized into two groups on the northeast side, while finer pebbles are concentrated in the northwest region. A belt of coarser clasts, though not as large as the two north-eastern groups, extends from the northeast towards the southwest. In the southernmost region of the gully, the majority of large boulders have been accurately detected despite the presence of interspersed patches of grass and shrubs. A notable error involves a sand and gravel bank being misidentified as a single large boulder. To prevent similar errors in the future, a mask generated through an image classification algorithm can be applied to exclude regions of the sediment obscured by sediment particles too fine for detection.

Figure 7a presents an aerial photograph of the entire catchment, with the three selected sample areas highlighted in red. The three areas were strategically selected within the belt of coarser clasts that extends from northeast to southwest to evaluate the algorithm's performance across a well-graded distribution of clast sizes. To visually assess the performance of the algorithm in each of the three sample areas, the detection map was superimposed onto corresponding aerial photography excerpts, enabling the identification and quantification of algorithm errors. To compare the distribution curves obtained, line sampling was conducted, mirroring the methodology employed by Fehr (1987). The left side of each panel features the automatically extracted distribution curves (red lines with blue error bars) alongside the manually produced curves (black lines). From left to right, the figure presents a snippet with highlighted detection errors, the detection map superimposed on the photographic snippet, and the manually performed line sampling, respectively.

The manually produced line (in black) falls within the error bounds of the algorithmic computation for a substantial portion of its length in all three samples, with only a few deviations. In Figure 7b, the manually generated distribution curve closely resembles the automatically derived one at the lower end of the spectrum, corresponding to clasts with a characteristic length below 30 cm. Beyond 30 cm, the manual distribution curve exhibits a noticeable gap compared to the automated curve, particularly in the 30-50 cm

diameter range. Considering that clasts in the 40th to 70th percentile of the automatically derived distribution exhibit well-graded dimensions, their color is expected to be represented by shades of green, yellow, and light orange. The cause of this discrepancy remains unclear. It could be attributed to excessive under-segmentation during the clast identification process. Alternatively, it could be due to a cluster of cobbles within this size range concentrated in the bottom left corner of the image. These cobbles, with few exceptions, fall outside the sample line. Two instances of under-segmentation exist, resulting in the misidentification of the larger diameter as the shorter one. One instance of under-segmentation leads to an overestimation of grain size, while another instance involves a partially covered large clast being misidentified as a smaller one. The under-segmentation instances arise from two clasts that are more frequently grouped together by the algorithm than separated. While a complete solution may not be feasible, future versions of the algorithm can significantly mitigate this issue. Addressing the over-segmented clast instance poses a greater challenge, as it necessitates post-processing steps involving convolutional neural networks (CNNs) or other artificial intelligence techniques to eliminate partially covered clasts when their characteristic length cannot be accurately determined. A notable observation can be made at the extreme lower end of the line sampling in Figure 7b, where the locations of the two smallest manual curve samples have been identified. The superimposed detection map confirms the accurate segmentation of the two small clasts, however, their relative distance appears to be exaggerated. This discrepancy between the photograph and the map is likely attributable to the coarse resolution of the mesh employed in the 3D confirmation process. Despite the successful detection in this particular instance, it is highly probable that numerous independent detections have been missed due to parallax error. Therefore, if these clasts had been more difficult to segment, potentially resulting in undetected instances by some vantage points, the subsequent loss of instance confirmations due to parallax error could have been detrimental to the overall detection process.

Figure 7c, derived from a more extensive sampling area encompassing a relatively finer grain size, exhibits a generally improved concordance between the manually and automatically generated curves. The manual

curve for this sample appears to overestimate the size of the smaller grains, particularly those in the lower half of the distribution with characteristic lengths below 30 cm, relative to the automatic curve. Nevertheless, the manual curve falls within the majority of uncertainty bands associated with the automatic detection. Consistent with the previous sample, the manually determined grain size distribution in this sample exhibits a noticeable gap within the range of 30 to 40 cm, albeit less evident. The coarser portion of the manual curve, encompassing grain sizes above the 90th percentile, exhibits an exceptionally good fit with the automatically generated curve. Figure 7 d exhibits the highest concordance among the three curves, with only a couple of minor deviations: in the 50 to 70 cm range and around the 20 cm range. In this sample, the automated method produces a visibly reduced density of detections compared to the other two, with ample areas, particularly in the upper half of the photograph (The most easterly region), remaining unmapped. This deterioration of performance can be readily explained by examining the 3D rendering of the gully (see Figure 3), as the upper portion of the d sample is situated upon a significantly steeper section of the sediment, consequently experiencing substantially more pronounced parallax errors arising from the mesh coarseness.

Across all three samples, the algorithm effectively refrains from detecting clasts in shrub-covered patches while still identifying those few grains that are visible through the vegetation. This accomplishment is noteworthy as no pre-processing mask was applied to eliminate vegetation or man-made objects. This underscores the inherent robustness of the method in handling such impediments.

4. Discussion

Grain size distribution (GSD) has been consistently recognized throughout the history of geological surveys as a fundamental characteristic of unconsolidated sediments. Complementing traditional physical measurement methods, photo-sieving has emerged as a valuable technique for expanding the spatial coverage and temporal resolution of GSD analysis in recent decades. Despite initial limitations, photo-sieving has undergone a rapid and multifaceted evolution, refining techniques and diversifying into various specialized applications. The primary distinction between photo-sieving methodologies lies in the use of object-based or statistical approaches, as exemplified in the introduction. In recent years, driven by

advancements in computing power and their overall superior performance, statistical methods have emerged as the most actively studied and rapidly evolving approach to photo-sieving. To our knowledge, the development of object-based methods peaked in 2012 with the release of the open-source tool BaseGrain. Despite their relative maturity, object-based methods offer several advantages, including the ability to produce continuous grain size distributions, the capability to measure large boulders, and the generation of more versatile, comprehensive, and informative data. This study contributes to the growing body of research utilizing object-based photo-sieving techniques and aims to advance the field in the following ways:

Texture-based or statistical methods directly generate a grain-size distribution (GSD) curve, whereas object-based approaches extract the GSD curve from an actual model of the surface grains. This capability enables object-based approaches to generate spatially continuous output and smooth curves, eliminating the need for binning and resulting in a more comprehensive and versatile dataset. Despite their advantages, object-based methods have historically exhibited lower accuracy, necessitating the development of post-processing techniques, such as the GUI approach proposed by Detert & Weitbrecht (2012), to *"handle of single grain elements within a post-processing"*. The requirement for manual post-processing has hitherto constrained object-based techniques to employ spatial sampling, hindering their ability to generate maps comparable to those presented by Lang et al. (2021). The method introduced in this study demonstrates that errors associated with the technique proposed by Detert & Weitbrecht (2012) can be alleviated by assessing the consistency of image-based detections over a 3D mesh. While accuracy can still be enhanced, this method eliminates the manual post-processing step previously required by the most advanced object-based techniques, expanding their detection capability by approximately two orders of magnitude.

The advent of this novel technique holds immense promise for the generation of a comprehensive training dataset for the Mask R-CNN image segmentation algorithm. These algorithms are typically trained on meticulously curated datasets comprising images with pixel-level annotations for object instances. By virtue of its object-based approach, our technique generates the precise pixel-level segmentation required for constructing a training dataset. Moreover, the comprehensive capture of objects from multiple points of view

generates a substantial volume of annotated images. While Mask R-CNNs have revolutionized the field of image segmentation, geological surveys have yet to fully harness the transformative power of this technology due to the scarcity of annotated data. Unlike cityscape-based datasets that have benefitted from the investment in self-driving cars and autonomous delivery systems, geological datasets remain largely untapped.

During the nascent stages of photo-sieving methodologies, (Ibbeken & Schleyer, 1986) postulated that *"The tails of the grainsize range such as cobbles or boulders, silt or clay, are almost impossible to sieve." " With the aid of photo-sieving, the surface grain-size distributions of larger sedimentary systems may be regularly mapped".* A significant advantage of photo-sieving lies in its capacity to effectively measure the dimensions of even the largest boulders. Notwithstanding their overall superior performance, as evidenced by comparative analyses (Harvey et al., 2022), statistically based methods exhibit limitations in accurately characterizing the largest values within a distribution curve. Addressing these limitations, Buscombe (2013) asserted that *"errors increase if insufficient numbers of grains are present* [in the picture]*",* while Lang et al. (2020) admitted that *"the performance deteriorates for very coarser gravel bars"* reasoning that this is *"caused by the high impact of individual large grains"*. The limitations in both these cases arise from the inherent requirement of these methods to extract the distribution curve from the texture of a photo, necessitating a set of specific image input characteristics. Images that deviate substantially from the reference images used during calibration, such as exhibiting significantly higher or lower resolutions, being captured from excessive heights, or containing unusually high or low particle counts, are likely to produce inaccurate output.

In contrast, the technique presented in this paper, which relies on brightness variations between particles and the intervening gaps, remains unaffected by the scale of the input photograph, whether in terms of drone flight altitude or image resolution. This characteristic confers upon our method a distinct advantage in mapping the coarser fraction of the grain size distribution, and despite certain technical limitations, enables our method to operate effectively across multiple orders of magnitude. The efficacy of our method in

measuring clasts of a specific size is intrinsically linked to the altitude at which the drone is operated. Flying the drone at higher altitudes enables the capture of larger clasts, while lower altitudes facilitate the resolution of finer grains. In the initial dataset employed for algorithm development, the one presented in this study, we operated the drone at an altitude of approximately 100 meters. This altitude enabled the capture of clasts with characteristic lengths exceeding 3 meters. However, the resolution of the method is insufficient to accurately measure particles smaller than pebbles.

A forthcoming line of inquiry, in addition to evaluating the method's performance on diverse sediments, will involve generating a series of datasets for a given sample at varying flight altitudes. This will serve to challenge the method's ability to span multiple orders of magnitude to its practical limit. While varying drone flight altitude expands the range of the GSD curve, it also introduces inherent technical limitations. A crucial requirement for SFM photogrammetry, the technique employed to generate a 3D mesh from a series of photographs (see section 2.2.2), is the overlap between images. This overlap ensures that the area captured by each photograph is represented in multiple images, enabling accurate reconstruction of the object's 3D structure. Image overlap also enables the critical process of 3D confirmation (see section 2.2.4), which involves comparing the same feature from different perspectives to verify its existence. Larger features are less likely to be fully contained within multiple images, potentially hindering this confirmation process. Consider an extreme scenario where a massive boulder fills the entire field of view of the camera in a particular image. In this case, even with significant overlap between images, the boulder may not be entirely captured in any other image, compromising the very possibility of 3D reconstruction. It becomes evident that small particles pose a challenge for the segmentation algorithm (as discussed in section 2.2.3), while large particles exhibit a reduced number of confirmations in the 3D confirmation algorithm (section 2.2.4). To maximize information acquisition while considering the terrain complexity, flight duration, battery limitations, and other technical constraints, it is crucial to optimize the drone's flight strategy and develop a data acquisition protocol able to adapt to various sediment characteristics. While the 3D confirmation algorithm likely necessitates further refinements, it can effectively operate in conjunction with

detection maps generated from imagery acquired at varying flight altitudes. This enables the confirmation of both large and small particles using complementary sets of detections applied to a shared mesh. Additionally, the drone can be equipped with cameras of varying focal lengths, allowing for the decoupling of physical flight altitude from the area captured in each image. In essence, the drone can acquire high-resolution images of smaller areas, suitable for capturing finer sediments, from significant altitudes by employing a camera with a longer focal length.

Texture-based approaches are also susceptible to degradation in the presence of confounding elements, such as vegetation or man-made artefacts, within the photographic sample. Buscombe (2013) asserted that *"the image should not contain non-sedimentary material, such as vegetation"*, elaborating further to specify that *"if the image covers a sufficient area, it can be sub-sampled (cropped) so as to avoid non-sedimentary material and the analyses performed on each sub-sample"*. The methodology proposed in this study exhibits fundamental robustness against vegetation and man-made objects due to the inherent variability in segmentation across different viewpoints. While a portion of the object may be segmented during the detection phase (section 2.2.3), the likelihood of consistent segmentation with identical features from diverse perspectives is extremely low. Consequently, these extraneous elements are effectively eliminated by the 3D confirmation algorithm (section 2.2.4). Misclassifications have occurred in instances where sand patches surrounded by vegetation have been erroneously identified as large boulders, as exemplified by the southernmost tip of the sediment deposit in the detection map depicted in Figure 6. While an image classification algorithm is still necessary to mask sand patches, there is no requirement to mask out vegetation or man-made objects. Additionally, the photographic sample does not need to be cropped to eliminate extraneous elements beyond the sediment itself.

5. Conclusions

The methodology presented here has effectively demonstrated that the synergistic integration of structure-from-motion photogrammetry with object detection-driven image segmentation techniques can significantly diminish segmentation errors and facilitate the realization of large-scale superficial grain size distribution

590 analysis. With further refinements, this technique has the potential to fulfil several of the stated objectives of
591 photo-sieving, including enhancing the spatial and temporal resolution of grain size distribution (GSD)
592 analysis and enabling the comprehensive mapping of clast size variability across surfaces. Despite its
593 nascent stage of development, the technique has exhibited remarkable efficacy, even in the presence of
594 under-segmentation and parallax errors. Further refinements in the 3D confirmation algorithm and the
595 implementation of a finer 3D mesh hold the promise of further enhancing its capabilities. The technique has
596 demonstrated remarkable resilience and adaptability in processing raw, unprocessed, and spatially extensive
597 samples characterized by the presence of abnormally large boulders, vegetation, and man-made artefacts.
598 Unlike texture-based approaches, our technique enables drone flights at varying altitudes, which, while
599 currently performed over a single height, holds the potential to achieve unprecedented GSD range, spanning
600 multiple orders of magnitude, from sub-centimeter to meter-scale characteristic lengths. Furthermore, the
601 technique's pixel-based annotation of a large number of images makes it exceptionally well-suited for
602 generating a training dataset for a future Mask R-CNN algorithm.

603 ## 6. Open Research

604 The software associated with this research are openly accessible on the GitHub repository at
605 https://github.com/DrLova/Grain-detection-for-landslides. Researchers and interested parties can access the
606 complete geological software code at this link for further exploration and validation. We encourage
607 collaboration and welcome inquiries regarding the provided resources at mlov@cdut.edu.cn

608 ## 7. Acknowledgements

609 This research is financially supported by the National Science Fund for Distinguished Young Scholars of
610 China (Grant 42125702), the Natural Science Foundation of Sichuan Province (Grant 22NSFSC0029), and
611 the Tencent Foundation through the XPLORER PRIZE (Grant XPLORER-2022-1012)

612

8. References

1. Adams, J. (1979). Gravel Size Analysis from Photographs. *Journal of the Hydraulics Division*, *105*(10), 1247–1255. https://doi.org/10.1061/JYCEAJ.0005283
2. Brasington, J., Vericat, D., & Rychkov, I. (2012). Modeling river bed morphology, roughness, and surface sedimentology using high resolution terrestrial laser scanning. *Water Resources Research*, *48*(11). https://doi.org/10.1029/2012WR012223
3. Bunte, K. (2001). *Sampling Surface and Subsurface Particle-size Distributions in Wadable Gravel- and Cobble-bed Streams for Analyses in Sediment Transport, Hydraulics, and Streambed Monitoring*. U.S. Department of Agriculture, Forest Service, Rocky Mountain Research Station.
4. Buscombe, D. (2013). Transferable wavelet method for grain-size distribution from images of sediment surfaces and thin sections, and other natural granular patterns. *Sedimentology*, *60*(7), 1709–1732. https://doi.org/10.1111/sed.12049
5. Buscombe, D. (2020). SediNet: A configurable deep learning model for mixed qualitative and quantitative optical granulometry. *Earth Surface Processes and Landforms*, *45*(3), 638–651. https://doi.org/10.1002/esp.4760
6. Buscombe, D., Rubin, D. M., & Warrick, J. A. (2010). A universal approximation of grain size from images of noncohesive sediment. *Journal of Geophysical Research: Earth Surface*, *115*(F2). https://doi.org/10.1029/2009JF001477
7. Butler, J. B., Lane, S. N., & Chandler, J. H. (2001). Automated extraction of grain-size data from gravel surfaces using digital image processing. *Journal of Hydraulic Research*, *39*(5), 519–529. https://doi.org/10.1080/00221686.2001.9628276
8. Carbonneau, P. e., Bizzi, S., & Marchetti, G. (2018). Robotic photosieving from low-cost multirotor sUAS: A proof-of-concept. *Earth Surface Processes and Landforms*, *43*(5), 1160–1166. https://doi.org/10.1002/esp.4298
9. Carbonneau, P. E., Lane, S. N., & Bergeron, N. E. (2004). Catchment-scale mapping of surface grain size in gravel bed rivers using airborne digital imagery. *Water Resources Research*, *40*(7).

https://doi.org/10.1029/2003WR002759

10. Casagli, N., Ermini, L., & Rosati, G. (2003). Determining grain size distribution of the material composing landslide dams in the Northern Apennines: Sampling and processing methods. *Engineering Geology*, *69*(1), 83–97. https://doi.org/10.1016/S0013-7952(02)00249-1
11. Detert, M., & Weitbrecht, V. (2012). Automatic object detection to analyze the geometry of gravel grains: A free stand-alone tool. *River Flow 2012 : Proceedings of the International Conference on Fluvial Hydraulics*, 595–600. https://www.research-collection.ethz.ch/handle/20.500.11850/63059
12. Dufresne, A., Bösmeier, A., & Prager, C. (2016). Sedimentology of rock avalanche deposits – Case study and review. *Earth-Science Reviews*, *163*, 234–259. https://doi.org/10.1016/j.earscirev.2016.10.002
13. Dunning, S. (2006). The grain size distribution of rock-avalanche deposits in valley-confined settings. *Italian Journal of Engineering Geology and Environment*, *1*, 117–121.
14. Fan, X., Dufresne, A., Whiteley, J., Yunus, A. P., Subramanian, S. S., Okeke, C. A. U., Pánek, T., Hermanns, R. L., Ming, P., Strom, A., Havenith, H.-B., Dunning, S., Wang, G., & Tacconi Stefanelli, C. (2021). Recent technological and methodological advances for the investigation of landslide dams. *Earth-Science Reviews*, *218*, 103646. https://doi.org/10.1016/j.earscirev.2021.103646
15. Fang, H. W., Liu, Y., & Stoesser, T. (2017). Influence of Boulder Concentration on Turbulence and Sediment Transport in Open-Channel Flow Over Submerged Boulders. *Journal of Geophysical Research: Earth Surface*, *122*(12), 2392–2410. https://doi.org/10.1002/2017JF004221
16. Fehr, R. (1987). Einfache Bestimmung der Korngrössenverteilung von Geschiebematerial mit Hilfe der Linienzahlanalyse. *Schweizer Ingenieur und Architekt*, *105*(38), 1104–1109. https://doi.org/10.5169/seals-76710
17. Graham, D. J., Reid, I., & Rice, S. P. (2005). Automated Sizing of Coarse-Grained Sediments: Image-Processing Procedures. *Mathematical Geology*, *37*(1), 1–28. https://doi.org/10.1007/s11004-005-8745-x
18. Graham, D. J., Rice, S. P., & Reid, I. (2005). A transferable method for the automated grain sizing of

river gravels. *Water Resources Research*, *41*(7). https://doi.org/10.1029/2004WR003868

19. Graham, D. J., Rollet, A.-J., Piégay, H., & Rice, S. P. (2010). Maximizing the accuracy of image-based surface sediment sampling techniques. *Water Resources Research*, *46*(2). https://doi.org/10.1029/2008WR006940
20. Habersack, H., Piegay, H., & Rinaldi, M. (2011). *Gravel Bed Rivers 6: From Process Understanding to River Restoration*. Elsevier.
21. Harvey, E. L., Hales, T. C., Hobley, D. E. J., Liu, J., & Fan, X. (2022). Measuring the grain-size distributions of mass movement deposits. *Earth Surface Processes and Landforms*, *47*(6), 1599–1614. https://doi.org/10.1002/esp.5337
22. He, J., Zhang, L., Fan, R., Zhou, S., Luo, H., & Peng, D. (2022). Evaluating effectiveness of mitigation measures for large debris flows in Wenchuan, China. *Landslides*, *19*(4), 913–928. https://doi.org/10.1007/s10346-021-01809-z
23. He, K., Gkioxari, G., Dollar, P., & Girshick, R. (2017). *Mask R-CNN*. 2961–2969. https://openaccess.thecvf.com/content_iccv_2017/html/He_Mask_R-CNN_ICCV_2017_paper.html
24. Hein, J. R. (2016). Manganese nodules. In *Encyclopedia of marine geosciences* (pp. 408–412). Dordrecht, the Netherlands: Springer.
25. Heritage, G. L., & Milan, D. J. (2009). Terrestrial Laser Scanning of grain roughness in a gravel-bed river. *Geomorphology*, *113*(1), 4–11. https://doi.org/10.1016/j.geomorph.2009.03.021
26. Huang, G.-H., Atkinson, P. M., & Wang, C.-K. (2018). Quantifying the scales of spatial variation in gravel beds using terrestrial and airborne laser scanning data. *Open Geosciences*, *10*(1), 607–617. https://doi.org/10.1515/geo-2018-0048
27. Ibbeken, H., & Schleyer, R. (1986). Photo-sieving: A method for grain-size analysis of coarse-grained, unconsolidated bedding surfaces. *Earth Surface Processes and Landforms*, *11*(1), 59–77. https://doi.org/10.1002/esp.3290110108
28. Irvine, G. V., Mann, D. H., & Short, J. W. (2006). Persistence of 10-year old Exxon Valdez oil on Gulf of Alaska beaches: The importance of boulder-armoring. *Marine Pollution Bulletin*, *52*(9),

1011–1022. https://doi.org/10.1016/j.marpolbul.2006.01.005

29. Lang, N., Irniger, A., Rozniak, A., Hunziker, R., Wegner, J. D., & Schindler, K. (2021). GRAINet: Mapping grain size distributions in river beds from UAV images with convolutional neural networks. *Hydrology and Earth System Sciences*, *25*(5), 2567–2597. https://doi.org/10.5194/hess-25-2567-2021
30. Li, M., Tang, C., Chen, M., & Gong, L. (2021). Formation and Vulnerability Analysis for Debris Flow Occurred on 20 August 2019 in Banzi Catchment, Wenchuan County, Sichuan Province, China. *Journal of Disaster Prevention and Mitigation Engineering*, *41*(2), 238–245.
31. Lovati, M. (2023). GRADELAND GitHub [software]. https://github.com/DrLova/Grain-detection-for-landslides
32. Lyu, X., You, Y., Li, D., Liu, J., Sun, H., & Liu, Y. (2022). Characteristics and Mitigation Measures of Banzi Gully Debris Flow on August 20th,2019，in Wenchuan County, Sichuan. *Journal of Disaster Prevention and Mitigation Engineering*, *42*(1), 12–23.
33. Meyer-Peter, E., & Müller, R. (1948). Formulas for Bed-Load transport. *IAHSR 2nd Meeting, Stockholm, Appendix 2*. https://repository.tudelft.nl/islandora/object/uuid%3A4fda9b61-be28-4703-ab06-43cdc2a21bd7
34. Roda-Boluda, D. C., D'Arcy, M., McDonald, J., & Whittaker, A. C. (2018). Lithological controls on hillslope sediment supply: Insights from landslide activity and grain size distributions. *Earth Surface Processes and Landforms*, *43*(5), 956–977. https://doi.org/10.1002/esp.4281
35. Sharma, K., Gold, M., Zurbrügg, C., Leal-Taixé, L., & Wegner, J. D. (2020). HistoNet: Predicting size histograms of object instances. *2020 IEEE Winter Conference on Applications of Computer Vision (WACV)*, 3626–3634. https://doi.org/10.1109/WACV45572.2020.9093484
36. Strom, A., Li, L., & Lan, H. (2019). Rock avalanche mobility: Optimal characterization and the effects of confinement. *Landslides*, *16*(8), 1437–1452. https://doi.org/10.1007/s10346-019-01181-z
37. Tritthart, M., Schober, B., & Habersack, H. (2011). Non-uniformity and layering in sediment transport modelling 1: Flume simulations. *Journal of Hydraulic Research*, *49*(3), 325–334.

https://doi.org/10.1080/00221686.2011.583528

38. Vázquez-Tarrío, D., Borgniet, L., Liébault, F., & Recking, A. (2017). Using UAS optical imagery and SfM photogrammetry to characterize the surface grain size of gravel bars in a braided river (Vénéon River, French Alps). *Geomorphology*, *285*, 94–105. https://doi.org/10.1016/j.geomorph.2017.01.039
39. Wang, D., You, Y., Li, D., Liu, J., Sun, H., Lyu, X., & Wang, Z. (n.d.). The river blockage characteristics of "8·20" large-scale debris flow and the hazard prediction in Banzi gully in Miansi Town， Wenchuan County. *The Chinese Journal of Geological Hazard and Control*, *33*(1), 59–66.
40. Warrick, J. A., Stevens, A. W., Miller, I. M., Harrison, S. R., Ritchie, A. C., & Gelfenbaum, G. (2019). World's largest dam removal reverses coastal erosion. *Scientific Reports*, *9*(1), Article 1. https://doi.org/10.1038/s41598-019-50387-7
41. Wolman, M. G. (1954). A method of sampling coarse river-bed material. *Eos, Transactions American Geophysical Union*, *35*(6), 951–956. https://doi.org/10.1029/TR035i006p00951
42. Woodget, A. S., Fyffe, C., & Carbonneau, P. E. (2018). From manned to unmanned aircraft: Adapting airborne particle size mapping methodologies to the characteristics of sUAS and SfM. *Earth Surface Processes and Landforms*, *43*(4), 857–870. https://doi.org/10.1002/esp.4285
43. Wu, F.-C., Wang, C.-K., & Huang, G.-H. (2018). Delineation of gravel-bed clusters via factorial kriging. *Geomorphology*, *308*, 161–174. https://doi.org/10.1016/j.geomorph.2018.02.013
44. Zhang, W., Liu, J., Li, D., You, Y., & Yang, H. (2023). Evaluation of comprehensive treatment effect of geotechnical and ecological engineering for debris flow: Case of Wenchuan County, Sichuan Province. *Natural Hazards*, *116*(1), 769–794. https://doi.org/10.1007/s11069-022-05698-w
45. Zhang, X., Tie, Y., Ning, Z., Yang, C., Li, Z., Li, M., Liang, J., Lu, J., Lu, T., Li, G., Li, G., & Xiang, B. (2023). Characteristics and activity analysis of the catastrophic "6•26" debris flow in the Banzi catchment, Wenchuan County of Sichuan Province. *HYDROGEOLOGY & ENGINEERING GEOLOGY*, *50*(5), 135–145.